This is the accepted manuscript made available via CHORUS. The article has been published as:

Exploring the exciton insulator state in math xmlns="http://www.w3.org/1998/Math/MathML">mrow>mn >1/mn>mtext>T-TiS/mtext>msub>mi mathvariant="normal">e/mi>mn>2/mn>/msub>/mrow>/ math> monolayer with advanced electronic structure methods

Hong Tang, Li Yin, Gábor I. Csonka, and Adrienn Ruzsinszky

Phys. Rev. B **111**, L201401 — Published 7 May 2025

DOI: 10.1103/PhysRevB.111.L201401

Exploring the Exciton Insulator State in 1T-$TiSe_2$ Monolayer with Advanced Electronic Structure Methods

Hong Tang[a], Li Yin, Gábor I. Csonka and Adrienn Ruzsinszky[b]

Department of Physics and Engineering Physics, Tulane University, New Orleans, LA 70118

ABSTRACT The layered transition metal dichalcogenide 1T-$TiSe_2$ is of great research interest, having intriguing properties of charge density waves (CDW) and superconductivity under doping or pressure. The monolayer form of 1T-$TiSe_2$ also shows a CDW with a higher transition temperature than the bulk, indicating a stronger CDW interaction. By using the meta-generalized gradient approximation (metaGGA)-based model Bethe-Salpeter Equation (mBSE) and many-body perturbation GW+BSE methods, we calculate the exciton binding energies and electron energy loss spectrum (EELS) for the 1T-$TiSe_2$ monolayer under different in-plane biaxial strains. We find that even without strain the 1T-$TiSe_2$ monolayer can have negative exciton energies at the Brillouin zone boundary point M, with a binding energy larger than the gap. The calculated EELS reinforces this picture, indicating EI (exciton insulator) states in 1T-$TiSe_2$ monolayer even without strain. The Wannier-Mott formula calculations of exciton binding energy corroborate results from GW+BSE. Small compressive strain enhances the EI state, and for tensile strains slightly less than 3%, the EI state in this monolayer persists. At large tensile strains, the material makes a transition to a normal semiconductor. Our results provide important information for understanding the quantum nature of this two-dimensional material. Our results from the standard

[a] Email: htang5@tulane.edu
[b] Email: aruzsin@tulane.edu

G_0W_0@PBE+SOC+U+BSE approach are not qualitatively different from those of a more computationally efficient metaGGA-based SCAN+SOC+U+mBSE+f_{xc}^{loc} approach that employs a model BSE.

Exciton insulator (EI) [1-4] is a state of matter in which electrons and holes spontaneously form bound excitons, due to strong electron-hole interactions. The formed bosonic excitons condense into Bose-Einstein condensates at low temperatures, forming a superfluid [5], an insulating electronic crystal [4, 6], or possibly a quantum liquid crystal [7,8]. Since the prediction of EI decades ago [1, 2], the search and verification of EI candidate materials have been of great interest and are actively ongoing, mainly driven by the fascinating macroscopic quantum phenomena and applications of EIs, such as superfluidity, perfect conductivity without a Meissner effect [8] and fractional Hall effects [9].

EI states can be realized in a bilayer quantum well under a high magnetic field [10-12], where the Landau level is vital for the EI formation and the electron and hole spatially reside in different layers, and in gate field tuned two-dimensional (2D) moiré heterostructures [13-15], in which EI is induced by the moiré flat bands instead of the dispersionless Landau levels. Also, great attention has been paid to the naturally formed EI states in equilibrium solid state materials without any external excitations and engineered structures, such as $TmSe_{0.45}Te_{0.55}$ [16,17], Ta_2NiSe_5 [18], 1T-$ZrTe_2$ [19,20] and 1T-$TiSe_2$ [21,22], featuring a semiconducting or semimetallic electronic configuration with a small band gap or a small overlap between valence and conduction bands, and a relatively weak screening effect for electrons and holes.

In EIs, the pairs of bound electrons and holes with different momenta form non-zero momentum excitons, and, after Bose condensation, the inverse of the exciton momentum sets a new length scale for charge spatial modulations, usually accompanied by a structural instability at this length scale concurrently. This apparent charge density wave (CDW) effect differs little from the one caused by Peierls instability (PI) [23] or Jahn-Teller distortion [24], which is driven by the electron-

phonon interaction. Bulk and monolayer 1T-$TiSe_2$ are among the intensely debated cases, regarding the EI or PI origination of the CDW phase transition [25-29]. The Angle-resolved photoemission spectroscopy (ARPES) experiment [30] on monolayer 1T-$TiSe_2$ found that its CDW transition temperature (T_{CDW}) is ~232K, higher than ~200 K of the bulk counterpart, indicating a more robust CDW phase in the monolayer, and suggesting an anisotropic order parameter in the bulk. A gap equation and critical temperature analysis from non-local density functional calculations [26] and a BCS-like exciton order parameter equation calculation [31] support the EI picture in 1T-$TiSe_2$. In contrast, calculations from anharmonic phonon [25] and quasi self-consistent GW [32] tend to support the PI picture, however, with overestimated T_{CDW} and backfolded conduction Ti d-orbitals at the Γ point, which are not observed in ARPES experiments [29, 30]. The experimentally observed coherent peaks in monolayer $TiSe_2$ on the highly oriented pyrolytic graphite (HOPG) substrate [27] favor an EI picture. For monolayer $TiSe_2$ on the MoS_2 substrate, the measured gap in the CDW phase is 120 meV, larger than that on HOPG, and the coherent peaks are absent, suggesting phase decoherence scattering from the substrate.

Strain engineering is effective in tuning material properties. Due to relatively high flexibility and strength, 2D materials can endure strains over 10% [33, 34], making properties (such as band gap (measured by STM/STS [35]), spin polarization [36], magnetism [37], optical spectrum [38-40], and exciton state [41]) adjustable dramatically, and enabling flexible, tunable and versatile applications. In this work, we explore the strain effect on the exciton binding energy in monolayer 1T-$TiSe_2$ by the advanced SCAN (strongly constrained and appropriately normed) metaGGA functional [42] within the framework of linear response time-dependent density functional theory (TDDFT) and many-body perturbation methods GW [43] with BSE (Bethe-Salpeter Equation) [44]. We find that in the normal phase without strain, the binding energy of the lowest energy

exciton formed by the hole at Γ and electron at M can be 380 meV, larger than the indirect gap 98 meV between Γ and M. The calculated EELS at different momentum transfer shows a soft mode like dispersion, indicating EI states existing in this monolayer. The EI state in the 1T-$TiSe_2$ monolayer is robust against in-plane strains, and it is enhanced even more with compressive strains, persisting up to about 3% of tensile strain. Our results provide an instrumental input to understanding and controlling the quantum properties of 1T-$TiSe_2$.

Computational and theoretical methods The G_0W_0 [43] and G_0W_0+BSE [44] calculations were performed in BerkeleyGW [43] with Quantum ESPRESSO [45]. The computational parameters and convergence test are shown in Note 2 in supplemental information (SI) [46]. The wavefunctions from PBE [48] +SOC+U (Perdew-Burke-Ernzerhof+spin-orbit-coupling+Hubbard U) were used for G_0W_0+BSE calculations, with U=4.45 eV. The Hubbard correction to PBE makes the bandgap of the unstrained monolayer 103 meV (see Figure S9), close to the experimental value of 98 meV at normal phase [30]. After the G_0W_0 calculation, the gap becomes about 0.9 eV. A scissor operation is applied to bring the gap close to the experimental value, keeping the G_0W_0 Fermi level unchanged, for the following BSE calculation. We found that the results are not sensitive to a slight change of the G_0W_0 Fermi level. The Fermi level is halfway between the top of the valence band and the bottom of the conduction band. The calculated band structure features around the Fermi level are similar to the experimental ones, such as the Se p-orbital valence band splitting around Γ and the overall band dispersion around the Fermi level and around Γ and M, indicating the correct relevant charge distribution, and hence capturing the important electrostatic effect in this monolayer. The Wannier-Mott formula [49] for exciton binding energy calculations is used to assess consistency of the results. We find that the SCAN+U+SOC+mBSE+f_{xc}^{loc} (see the following paragraphs) and G_0W_0+BSE results are consistent. We note that PBE+SOC+U with

U=2.5 eV, turns the unstrained monolayer into a metal, but after the G_0W_0 calculation, it becomes semiconducting with an indirect gap of 103 meV, close to the experimental. The Wannier-Mott formula calculation of exciton binding energy for this case also leads to a result consistent with the results obtained by the methods applied in this paper. Table S1 shows the calculated gaps with PBE+SOC+U and G_0W_0@PBE+SOC+U with different U values.

Our TDDFT-based approximation resembles the model BSE (mBSE) method [50-52] in the construction of the screening (see Note 2 in [46]). mBSE and TDDFT are both based on the Casida equation formalism. The algorithm for solving the Casida equation [53] is very similar to that for the Bethe-Salpeter equation (BSE) [44]. In the standard GW+BSE approach to optical absorption, one first computes a GW quasiparticle band structure, an expensive step scaling as N^4 [52] where N is the number of electrons, and then uses that to construct a frequency-dependent dielectric function with off-diagonal matrix elements. Here we employ a one-shot SCAN+U functional, with the efficiency of a semi-local metaGGA and with U fitted to yield the experimental band gap. SCAN+U replaces the originally proposed hybrid functional by A. Tal et al [52]. Because SCAN satisfies 17 exact constraints [42], while PBE satisfies only 9, and because SCAN satisfies more appropriate norms, U is typically smaller for SCAN than for PBE. At a much lower cost, SCAN+U can perform like a hybrid functional for difficult problems [54].

The mBSE model screening is built on the dielectric function from G_0W_0@SCAN+SOC+U. We did not achieve the full speed-up over GW+BSE that Ref. 52 achieved by the dielectric dependent hybrid functional [52,55], but our choice appears to be a safer technique since we did extend beyond three dimensional *sp* solids to the 2D transition-metal dichalcogenide 1T-$TiSe_2$, including the spin-orbit correction (SOC). We compute a static $1/\varepsilon_\infty(q)$ from G_0W_0@SCAN+SOC+U and

determine the two parameters by fitting the diagonal $1/\varepsilon_\infty(q)$ to a simple model. α and μ are obtained from a fitting of the static dielectric function with the following model [52],

$$\varepsilon^{-1}(q) = 1 - (1-\alpha)\exp\left(-\frac{q^2}{4\mu^2}\right), \quad (1)$$

where q is the length of wavevector. The values of α and μ are 0.329 and 0.62, respectively, for 1T-$TiSe_2$ monolayer (Figure S14 in [46]).

In the standard GW+BSE approach to optical absorption, the absorption frequencies are found as generalized eigenvalues of an equation like the Casida equation of TDDFT, involving a screened exchange matrix element between pairs of one-electron Bloch states. In our approach, we keep only the diagonal elements of the corresponding dielectric matrix (which is a computational saving since the diagonal of the matrix is much smaller than the whole matrix), ignore the frequency dependence, and model the effect of the off-diagonal matrix elements or local-field effects by a short-ranged static exchange-correlation kernel f_{xc}^{loc}, depending as in Ref. 52 on the parameters α and μ.

We denote this method as SCAN+U+mBSE+f_{xc}^{loc} where f_{xc}^{loc} is a local exchange-correlation kernel built up from the SCAN meta-GGA. The local-field effects from f_{xc}^{loc} were found to have minor impact in bulk solids [52] but they could be more important in low-dimensional materials. MetaGGA-based kernels are a promising direction for excitonic effects [56-59].

Strain effects on exciton binding energies The atomic structure and the calculated band structures of the 1T-$TiSe_2$ monolayer are shown in Figures S1(a)-(f) in the Supporting Information (SI) [46]. The computational parameters are shown in Notes 1 and 2 in SI [46]. The conduction bands arise mainly from Ti 3d-orbitals while the valence bands around the Fermi level are from Se

4p-orbitals, consistent with previous calculations [30, 31], and with the results of bulk 1T-$TiSe_2$ [63]. The spin of the top of the valence band around Γ, contributed from the Se p-orbital, is mainly oriented along the z axis, while the conduction band minimum around M, contributed from the Ti d-orbital, is mainly oriented along the x-y plane (see Figures S1(d)-(f) in [46]). Figures 1a-d show the quasiparticle and the first (lowest energy) exciton band structures along the Γ-M direction, under different strains, calculated from G_0W_0(@PBE+SOC+U 4.45 eV)+BSE. For compressive 0.25%, zero, and 2% tensile strains, we find a portion of the exciton bands below VBM (valence band maximum), indicating negative exciton energies and hence larger exciton binding energies than the quasiparticle gaps at M. Excisions can be formed spontaneously under these strain conditions, without any excitation energies, indicating that the EI state is the ground state. For 3% tensile strain, the exciton band is all above the VBM, and a non-zero excitation energy is needed to excite excitons, showing a normal semiconducting state. Figures 1e and 1f show the changing trend of the quasiparticle gaps and the first exciton binding energies at M with strains. Figure 1e is the results from G_0W_0(@PBE+SOC+U)+BSE (U=4.45 eV) and Figure 1f shows results from SCAN+SOC+U+mBSE+f_{xc}^{loc} (U=3.81 eV). They both show almost linear dependences on the gap and exciton binding energy with the applied strains from compressive 0.25% to tensile 4%. The G_0W_0(@PBE+SOC+U)+BSE method predicts that below the tensile strain of 2.75%, the binding energy of the exciton is larger than the gap. Beyond that strain, the gap becomes larger, indicating an EI state below strains of 2.75%, and a normal semiconducting state above strains of 2.75%. The calculated exciton binding energy from SCAN+SOC+U+mBSE+f_{xc}^{loc} is about 40 meV lower than that from G_0W_0(@PBE+SOC+U)+BSE, making the EI to semiconducting transition strain value slightly smaller (about tensile 2.66%). The calculated relatively large binding energy (~360-460 meV) of the exciton with a momentum transfer from Γ to M indicates a strong interaction between

electrons and holes in monolayer 1T-$TiSe_2$, consistent with the reduced screening effect from the reduced dimensionality of the 2D layer. A negligible difference (< 1 meV) in the calculated exciton energies is found in the mBSE calculation without the f_{xc}^{loc} term, consistent with the results in Ref. 52 for isotropic systems, and echoing the isotropy in the 2D plane of monolayer $TiSe_2$.

The exciton binding energy can be estimated by the Wannier-Mott formula $E_b = -(m_\mu * Ry)/\varepsilon_r^2$, where $m_\mu = (m_e \cdot m_h)/(m_e + m_h)$ is the reduced mass, m_e and m_h are the effective masses the electron at the conduction band minimum and the hole at the valence band maximum, respectively. Ry=13.6 eV and ε_r is the dielectric constant of the system as referred to vacuum, at the wavevector of the exciton. The calculated binding energy of the first exciton with momentum transfer from Γ to M is shown in Table S1 in SI [46]. The estimated exciton binding energies from the Wannier Mott model are close to the results from standard G_0W_0(@PBE+SOC+U)+BSE and the new SCAN+SOC+U+mBSE+f_{xc}^{loc}, as shown in Figure 1; all fall in the range of ~350-520 meV, larger than the band gap (~100meV) of the unstrained monolayer. For G_0W_0(@PBE+SOC+U), with U = 2.5 eV, the PBE+SOC+U calculation results indicate a metallic state for the unstrained 1T-$TiSe_2$ monolayer, with an overlap of approximately 310 meV between the VBM at Γ and the CBM at M. After the G_0W_0 calculation, the material becomes semiconducting with an indirect gap of 103 meV between Γ and M. By using the Wannier function interpolation [64] of the calculated G_0W_0 band structure, the masses of the electron at M and hole at Γ can be determined. Using the Wannier-Mott formula, the exciton binding energy with momentum transfer from Γ to M is predicted to be 303 meV for G_0W_0@PBE+SOC+U (U = 2.5 eV), still close to the values determined by the other methods considered in this work. This consistency of the calculated exciton binding energies with different methods confirms the strong interaction between electron and hole and the EI states in this monolayer.

With the strain altering from compressive 0.25% to tensile 3%, the band gap between Γ and M is increasing from about 60 meV to about 500 meV (see Note 3 in SI [46] for the discussion of the changing trend of band gap with strains). Compared with the large change of the band gap with strains, the exciton binding energy change is relatively small, only about 10%, indicating a small change in the effective mass of the exciton and the screening effect, and the robust exciton states in the monolayer.

Electron energy loss (EELS) and plasmon dispersion Figure 2 shows the calculated EELS [67] curves of different momentum transfer of the unstrained 1T-$TiSe_2$ monolayer. The onset frequency of each EELS curve at different momentum transfer (q1, q2, …), indicated by the dashed black lines, represents the starting point of the energy loss due to creations of excitons with that momentum. The curve q1 represents zero momentum transfer of electron and hole in the exciton formation, q2 for a momentum transfer of $\frac{1}{9}Q_{\mathrm{M}}$, etc. where Q_{M} is the length from Γ to M in Brillouin zone (BZ). The positive EELS at the onset frequencies, in the curves q1-q5 of figure 2, corresponds to energy inputs needed to excite excitons (or plasmons [68-73]) with those momenta. The EELS curves q6–q10 show anomalous features around zero frequency in Figure 2, indicating that energy may be gained by exciting excitons with those momenta. . This anomaly reflects that the binding energy of excitons is already larger than the gap, and no energy input is needed to excite excitons. The EI state can spontaneously form in the material.

The EELS curves under compressive and tensile strains are shown in Figure S17 in SI [46]. The onset frequencies of curves q1-q5 under compressive 0.25% are slightly smaller than those of the unstrained one. The curves of q6-q10 also show an anomaly around zero frequency, indicating that the EI state can also spontaneously form at a compressive strain of 0.25%. For a tensile strain of 2% (Figure S17c in [46]), the onset frequencies of curves q1-q5 are even increased, and the EELS

curves of q6 and q7 become positive at the onset frequencies. Only the curves of q8-q10 show a soft-mode like feature around zero frequency. This reflects the fact that the increase of the gap induced by tensile strains is faster than the increase of exciton binding energy, as shown in figure 1, so, the range of q points with negative exciton energies is shrinking with tensile strains, as shown in figure 1c. At the tensile strain of 2%, the monolayer also forms the EI state. With the tensile strain increased to 3%, all the EELS curves turn to positive at the onset frequencies around zero frequency, although the onset frequencies for curves q9 and q10 are small. This means an unspontaneous EI state. To excite excitons with all momenta, an energy input is required. Therefore, the monolayer behaves as a normal semiconductor, and the EI state cannot form. One can observe strain induced EI-to-semiconducting phase transition in this monolayer.

The onset frequencies of the calculated EELS curves with small momentum transfers (q1-q3) of the unstrained monolayer in Figure 2 show an increasing trend with small momentum transfer q values. This is qualitatively consistent with experiments of the bulk 1T-$TiSe_2$ [21, 74], where at the normal phase, the low energy plasmon frequency increases with q at small q values, while with increasing q, the low energy plasmon peak is quickly undiscernible due to the strong decay induced by the Landau damping [75]. Monolayer 1T-$TiSe_2$ is slightly different from its bulk counterpart. Due to the strong quantum confinement effect, the Ti d-orbitals repel the Se p-orbitals, and form a relatively larger gap (~100 meV) in the monolayer, while in the bulk, $TiSe_2$ either has a smaller gap or is semimetal with both electron and hole pockets around the Fermi level in the normal phase [76]. Possible interband transitions from different layers in the bulk case are absent in the monolayer. This leads to quantitatively different low energy plasmon frequencies and possibly different trends with q.

Figures 3a-3f show the exciton spectra for different momentum transfer of the unstrained 1T-$TiSe_2$ monolayer. The first (lowest energy) excitons are all dark excitons. However, for small momentum transfer (see Figures 3a and 3b), there are bright excitons with energies very close to those of the first dark exciton. In this small momentum transfer region, these almost degenerate bright and dark excitons may be useful for manipulating quantum information. The formed lowest energy dark excitons reflect the fact that the hole from the top of valence band has spin mainly polarized in the z direction, while the spins of the electrons in the lowest conduction band are mainly polarized in the x-y plane. The relatively large lifetime of these dark excitons may also be a useful tool for important quantum manipulations. Furthermore, Figures 3(g)-3(l) show that those dark excitons have a very concentrated distribution in the momentum space. Figures 3(m)-3(n) show the modulus squared of the real-space exciton wavefunction of the lowest energy exciton at momentum transfer q1=0, showing a relatively large spatial distribution and a circular shape with a radius of about 1-2 nm. Figures 3(o)-3(p) show the spatial distribution of the exciton wave function of the lowest energy exciton at q10=$1.0Q_{\mathrm{M}}$, showing a delocalization feature in real-space. This wavefunction delocalization feature also occurs in monolayer transition metal dichalcogenide topological exciton insulators [77].

In conclusion, we calculated the exciton binding energies and EELS for monolayer 1T-$TiSe_2$ under different in-plane strains with a SCAN metaGGA based model BSE with local f_{xc}, and many-body perturbation GW+BSE methods. The consistent results from the two methods imply that they both capture the same physics for the exciton binding in this material. SCAN+U+mBSE+f_{xc}^{loc} appears as a promising and computationally more feasible alternative to GW+BSE. We found that even without strains, the monolayer 1T-$TiSe_2$ can exhibit negative exciton energies at the BZ boundary point M. Those excitons with larger binding energy than the gap can be formed

spontaneously without any external energy input. The calculated EELS also reinforces this picture, indicating that the monolayer 1T-$TiSe_2$ is an EI even without any strain. The exciton binding energy calculations from the Wannier-Mott formula also deliver consistent results. Small compressive strains enhance this EI picture for this monolayer, and even for tensile strains of about a little bit less than 3%, the EI state in this monolayer persists. At large tensile strains, the 1T-TiSe monolayer transitions to a normal semiconductor. The gap tunability by strain can be ~120 meV/% in 1T-$TiSe_2$ monolayer, indicating a promising application in novel electronic devices with high flexibility. Our results provide important information for understanding the quantum nature of this amazing 2D material.

ACKNOWLEDGEMENTS

The authors thank the discussion with Prof. John P. Perdew and his valuable suggestions. This work was supported by the donors of ACS Petroleum Research Fund under New Directions Grant 65973-ND10. A.R. served as Principal Investigator on ACS PRF 65973-ND10 that provided support for H.T. L.Y. and A.R. acknowledge support from Tulane University's startup fund, which also supports L.Y. This research includes calculations carried out on HPC resources supported in part by the National Science Foundation through major research instrumentation grant number 1625061 and by the US Army Research Laboratory under contract number W911NF-16-2-0189. This research was supported in part by the high performance computing (HPC) resources and services provided by Information Technology at Tulane University, New Orleans, LA.

References

1. N. F. Mott, The transition to the metallic state, Philos. Mag. **6**, 287–309 (1961).
2. L. V. Keldysh, Y. V. Kopaev, Possible Instability of the Semimetallic State toward Coulomb Interaction, Sov. Phys. Solid State **6**, 2219–2224 (1965).
3. B. I. Halperin, T. M. Rice, Possible Anomalies at a Semimetal-Semiconductor Transition, Rev. Mod. Phys. **40**, 755–766 (1968).
4. W. Kohn, D. Sherrington, Two Kinds of Bosons and Bose Condensates, Rev. Mod. Phys. **42**, 1–11 (1970).
5. D. Snoke, Spontaneous Bose coherence of excitons and polaritons, Science **298**, 1368 (2002).
6. D. Jérome, T. M. Rice, and W. Kohn, Excitonic insulator, Phys. Rev. **158**, 462 (1967).
7. S. Kivelson, E. Fradkin, and V. Emery, Electronic liquid-crystal phases of a doped Mott insulator, Nature (London) **393**, 550 (1998).
8. A. J. Beekman, J. Nissinen, K. Wu, and J. Zaanen, Dual gauge field theory of quantum liquid crystals in three dimensions, Phys. Rev. B **96**,165115 (2017).
9. Y. Hu, J. W. Venderbos, and C. Kane, Fractional Excitonic Insulator. Phys. Rev. Lett. **121**, 126601 (2018).
10. J. P. Eisenstein, A. H. Macdonald, Bose-Einstein condensation of excitons in bilayer electron systems, Nature **432**, 691 (2004).
11. J. P. Eisenstein, Exciton Condensation in Bilayer Quantum Hall Systems, Annu. Rev. Condens. Matter Phys. **5**, 159–181 (2014).
12. J. I. A. Li, T. Taniguchi, K. Watanabe, J. Hone, and C. R. Dean, Excitonic superfluid phase in double bilayer graphene. Nat. Phys. **13**, 751–755 (2017).

13. D. Chen, Z. Lian, X. Huang, Y. Su, M. Rashetnia, L. Ma, L. Yan, M. Blei, L. Xiang, T. Taniguchi, K. Watanabe, S. Tongay, D. Smirnov, Z. Wang, C. Zhang, Y.-T. Cui and S.-F. Shi, Excitonic insulator in a heterojunction moiré superlattice, Nature Physics **18**, 1171–1176 (2022).
14. J. Gu, L. Ma, S. Liu, K. Watanabe, T. Taniguchi, J. C. Hone, J. Shan and K. F. Mak, Dipolar excitonic insulator in a moiré lattice, Nature Physics **18**, 395–400 (2022).
15. Z. Zhang, E. C. Regan, D. Wang, W. Zhao, S. Wang, M. Sayyad, K. Yumigeta, K. Watanabe, T. Taniguchi, S. Tongay, M. Crommie, A. Zettl, M. P. Zaletel and F. Wang, Correlated interlayer exciton insulator in heterostructures of monolayer WSe2 and moiré WS2/WSe2, Nature Physics **18**, 1214–1220 (2022).
16. B. Bucher, P. Steiner, and P. Wachter, Excitonic Insulator Phase in TmSe0.45Te0.55. Phys. Rev. Lett. **67**, 2717–2720 (1991).
17. P. Wachter, Exciton condensation in an intermediate valence compound: TmSe0.45Te0.55. Solid State Commun. **118**, 645–650 (2001).
18. Y. F. Lu, et al. Zero-gap semiconductor to excitonic insulator transition in Ta2NiSe5. Nat. Commun. **8**, 14408 (2017).
19. M. Q. Ren, et al. Semiconductor-Metal Phase Transition and Emergent Charge Density Waves in 1T-ZrX2(X = Se, Te) at the Two Dimensional Limit. Nano Lett. **22**, 476–484 (2022).
20. Y. Song, C. Jia, H. Xiong, B. Wang, Z. Jiang, K. Huang, J. Hwang, Z. Li, C. Hwang, Z. Liu, D. Shen, J. A. Sobota, P. Kirchmann, J. Xue, T. P. Devereaux, S.-K. Mo, Z.-X. Shen and S. Tang, Signatures of the exciton gas phase and its condensation in monolayer 1T-ZrTe2, Nature Communications **14**, 1116 (2023).

21. A. Kogar, et al. Signatures of exciton condensation in a transition metal dichalcogenide. Science **358**,1314–1317 (2017).
22. T. Rohwer, et al. Collapse of long-range charge order tracked by time-resolved photoemission at high momenta. Nature **471**, 490–493 (2011).
23. G. Grüner, Density Waves in Solids (Perseus Books, New York, 2000).
24. K. Rossnagel, L. Kipp, and M. Skibowski, Charge-density wave phase transition in 1T-TiSe2: Excitonic insulator versus band-type Jahn-Teller mechanism, Phys. Rev. B **65**, 235101 (2002).
25. J. S. Zhou, L. Monacelli, R. Bianco, I. Errea, F. Mauri, and M. Calandra, Anharmonicity and Doping Melt the Charge Density Wave in Single-Layer TiSe2, Nano Lett. **20**, 4809-4815 (2020).
26. H.-Y. Chen, T. Nomoto, and R. Arita, Development of an ab initio method for exciton condensation and its application to TiSe2, Physical Review Research **5**, 043183 (2023).
27. S. Kolekar, M. Bonilla, Y. Ma, H. C. Diaz, and M. Batzill, Layer and substrate-dependent charge density wave criticality in 1T−TiSe2, 2D Mater. **5**, 015006 (2018).
28. B. Guster, E. Canadell, M. Pruneda, and P. Ordejón, First principles analysis of the CDW instability of single-layer 1T-TiSe2 and its evolution with charge carrier density, 2D Mater. **5**, 025024 (2018).
29. P. Chen, Y.-H. Chan, M.-H. Wong, X.-Y. Fang, M. Y. Chou, S.-K. Mo, Z. Hussain, A.-V. Fedorov, and T.-C. Chiang, Dimensional Effects on the Charge Density Waves in Ultrathin Films of TiSe2, Nano Lett. **16**, 6331-6336 (2016).

30. P Chen, Y. -H. Chan, X. -Y. Fang, Y Zhang, M Y Chou, S. -K. Mo, Z Hussain, A. -V. Fedorov and T. -C. Chiang, Charge density wave transition in single-layer titanium diselenide, Nature Commu. **6**, 8943 (2015).
31. J. M. Bok, J. Hwang, and H.-Y. Choi, Excitonic insulator emerging from semiconducting normal state in 1T-TiSe2, Phys. Rev. B **103**, 205108 (2021).
32. Ross E. Larsen, Dimitar Pashov, Matthew D. Watson, Swagata Acharya, Mark van Schilfgaarde, Lattice fluctuations, not excitonic correlations, mediated electronic localization in TiSe2, arXiv:2311.08015
33. C. Lee, X. Wei, J. W. Kysar, J. Hone, Measurement of the Elastic Properties and Intrinsic Strength of Monolayer Graphene. Science **321**, 385–388 (2008).
34. S. Bertolazzi, J. Brivio, and A. Kis, Stretching and Breaking of Ultrathin MoS2, ACS nano **5**, 9703-9709 (2011).
35. D. J. Trainer, Y. Zhang, F. Bobba, X. Xi, S.-W. Hla, and M. Iavarone, The Effects of Atomic-Scale Strain Relaxation on the Electronic Properties of Monolayer MoS2, ACS Nano **13**, 8284−8291 (2019).
36. H. Tang, S. Neupane, L. Yin, J. M. Breslin and A. Ruzsinszky, Spin-polarization anisotropy controlled by bending in tungsten diselenide nanoribbons and tunable excitonic states, J. Mater. Chem. C **11**, 4711 (2023).
37. H. Tang, S. Neupane, Q. Yan and A. Ruzsinszky, Density Functional Theory Study of Controllable Optical Absorptions and Magneto-Optical Properties of Magnetic CrI3 Nanoribbons: Implications for Compact 2D Magnetic Devices, ACS Applied Nano Materials **5**, 14388–14399 (2022).

38. K. Zollner, P. E. Faria Junior and J. Fabian, Strain-Tunable Orbital, Spin-Orbit, and Optical Properties of Monolayer Transition-Metal Dichalcogenides, Phys. Rev. B **100**, 195126 (2019).

39. R. Frisenda, M. Drüppel, R. Schmidt, S. M. de Vasconcellos, D. P. de Lara, R. Bratschitsch, M. Rohlfing and A. Castellanos-Gomez, Biaxial Strain Tuning of the Optical Properties of Single-Layer Transition Metal Dichalcogenides, npj 2D Mater. Appl. **1**, 10 (2017).

40. P. E. Faria Jr., K. Zollner, T. Wozniak, M. Kurpas, M. Gmitra and J. Fabian, First-Principles Insights into the Spin-Valley Physics of Strained Transition Metal Dichalcogenides Monolayers, New J. Phys. **24,** 083004 (2022).

41. H. Tang, B. Neupane, S. Neupane, S. Ruan, N. K. Nepal and A. Ruzsinszky, Tunable band gaps and optical absorption properties of bent MoS2 nanoribbons, *Scientific Reports,* **12**, 3008 (2022).

42. J. Sun, A. Ruzsinszky, and J. P. Perdew, Strongly Constrained and Appropriately Normed Semilocal Density Functional, Phys. Rev. Lett. **115**, 036402 (2015).

43. J. Deslippe, G. Samsonidze, D. A. Strubbe, M. Jain, M. L. Cohen and S. G. Louie, BerkeleyGW: A Massively Parallel Computer Package for the Calculation of the Quasiparticle and Optical Properties of Materials and Nanostructures, Comput. Phys. Commun. **183**, 1269 (2012).

44. M. Rohlfing and S. G. Louie, Electron-Hole Excitations and Optical Spectra from First Principles, Phys. Rev. B, **62**, 4927 (2000).

45. P. Giannozzi, O. Andreussi, T. Brumme, O. Bunau, M. Buongiorno Nardelli, M. Calandra, R. Car, C. Cavazzoni, D. Ceresoli, M. Cococcioni, N. Colonna, I. Carnimeo, A. Dal Corso, S. de Gironcoli, P. Delugas, R. A. DiStasio Jr, A. Ferretti, A. Floris, G. Fratesi, G. Fugallo,

R. Gebauer, et al. Advanced Capabilities for Materials Modelling with Quantum ESPRESSO, J. Phys.: Condens. Matter. **29**, 465901 (2017).

46. Supplemental information: computational parameters and convergence tests, potentials in metaGGA+mBSE, fitting α and μ and graphs, atomic structures of monolayer 1T-TiSe2, fat band structures of monolayer 1T-TiSe2 under different strains, spin polarization resolved band structures under different strains, graph of trigonal antiprism (or octahedron), PDOS plots of monolayer 1T-TiSe2 under different strains, and tables of relevant bond angles, lengths, and band widths under different strains.
47. J. Deslippe, G. Samsonidze, M. Jain, M. L. Cohen, and S. G. Louie, Coulomb-hole summations and energies for GW calculations with limited number of empty orbitals: A modified static remainder approach, Phys. Rev. B **87**, 165124 (2013).
48. J. P. Perdew, K. Burke, M. Ernzerhof, Generalized Gradient Approximation Made Simple, Phys. Rev. Lett. **77**, 3865 (1996).
49. G. H. Wannier, The Structure of Electronic Excitation Levels in Insulating Crystals, Phys. Rev. **52,** 191 (1937).
50. M. Bokdam, T. Sander, A. Stroppa, S. Picozzi, D. D. Sarma, C. Franchini, and G. Kresse, Role of Polar Phonons in the Photo Excited State of Metal Halide Perovskites, Scientific Reports **6**, 28618 (2016).
51. P. Liu, B. Kim, X.-Q. Chen, D. D. Sarma, G. Kresse, and C. Franchini, Relativistic GW+BSE study of the optical properties of Ruddlesden-Popper iridates, Phys. Rev. Materials **2**, 075003 (2018).

52. A. Tal, P. Liu, G. Kresse, and A. Pasquarello, Accurate optical spectra through time-dependent density functional theory based on screening-dependent hybrid functionals, Phys. Rev. Research **2**, 032019(R) (2020).

53. M. E. Casida, Time-dependent density-functional response theory for molecules, in Recent Advances in Density Functional Methods, Part I, edited by D. P. Chong, page 155, World Scientific, Singapore, 1995.

54. R. K. Sah, M. J. Zdilla, E. Borguet, and J. P. Perdew, Meta-GGas vs. Hybrid Functionals for Point Defects: The Best of Both Worlds Applied to Layered MnO2 and KCoO2, arXiv: 2024. 14317v3[physics.comp-ph]

55. W. Chen, G. Miceli, G.M. Rignanese, and A. Pasquarello, Nonempirical dielectric-dependent hybrid functional with range separation for semiconductors and insulators, Phys. Rev. Mater. **2**, 073803 (2018).

56. B. Himmetoglu, A. Floris, S. de Gironcoli, and M. Cococcioni, Hubbard-corrected DFT energy functionals: The LDA+U description of correlated systems, Int. J. Quantum Chem. **114**, 14 (2014).

57. J. Paier, M. Marsman, and G. Kresse, Dielectric properties and excitons for extended systems from hybrid functionals, Phys. Rev. B **78**, 121201 (2008).

58. A. M. Ferrari, R. Orlando, and M. Rerat, Ab Initio Calculation of the Ultraviolet–Visible (UV-vis) Absorption Spectrum, Electron-Loss Function, and Reflectivity of Solids, J. Chem. Theory Comput. **11**, 3245 (2015).

59. V. U. Nazarov and G. Vignale, Optics of Semiconductors from Meta-Generalized-Gradient-Approximation-Based Time-Dependent Density-Functional Theory, Phys. Rev. Lett. **107**, 216402 (2011).

60. G. Kresse and J. Furthmüller, Efficient Iterative Schemes for Ab Initio Total-Energy Calculations Using a Plane-Wave Basis Set, Phys. Rev. B **54**, 11169 (1996).

61. G. Kresse and D. Joubert, From Ultrasoft Pseudopotentials to the Projector Augmented-Wave Method, Phys. Rev. B **59**, 1758 (1999).

62. X.-Y. Fang, H. Hong, P. Chen, and T.-C. Chiang, X-ray study of the charge-density-wave transition in single-layer TiSe2, Phys. Rev. B **95**, 201409(R) (2017).

63. M. Hellgren, J. Baima, R. Bianco, M. Calandra, F. Mauri, and L. Wirtz, Critical Role of the Exchange Interaction for the Electronic Structure and Charge-Density-Wave Formation in TiSe2, Phys. Rev. Lett. **119**, 176401 (2017).

64. G. Pizzi, V. Vitale, R. Arita, S. Blügel, F. Freimuth, G. Géranton, M. Gibertini, D. Gresch, C. Johnson, T. Koretsune, J. Ibañez-Azpiroz, H. Lee, J.M. Lihm, D. Marchand, A. Marrazzo, Y. Mokrousov, J.I. Mustafa, Y. Nohara, Y. Nomura, L. Paulatto, S. Poncé, T. Ponweiser, J. Qiao, F. Thöle, S.S. Tsirkin, M. Wierzbowska, N. Marzari, D. Vanderbilt, I. Souza, A.A. Mostofi, J.R. Yates, Wannier90 as a community code: new features and applications, J. Phys. Cond. Matt. 32, 165902 (2020).

65. H. J. Conley, B. Wang, J. I. Ziegler, R. F. Haglund, Jr., S. T. Pantelides, and K. I. Bolotin, Bandgap Engineering of Strained Monolayer and Bilayer MoS2, Nano Lett. **13**, 3626−3630 (2013).

66. M. Chhowalla, H. S. Shin, G. Eda, L.-J. Li, K. P. Loh, and H. Zhang, The chemistry of two-dimensional layered transition metal dichalcogenide nanosheets, Nature Chemistry **5**, 263–275 (2013).

67. J. Hillier, R. F. Baker, Microanalysis by Means of Electrons, J. Appl. Phys. **15**, 663–675 (1944).

68. In a real experiment, due to the small gap (~100 meV) of monolayer 1T-$TiSe_2$ and possible carrier doping from defects or substrates, low carrier density physics may come into play, like ghost modes [Ref. 69], which are due to imperfect screening of the electron-hole interaction at short distances [Refs. 70-73], featuring in negative static screening, and have mixed features of exciton and plasmon.
69. J. Koskelo, L. Reining, and M. Gatti, Short-range excitonic phenomena in low-density metals, arXiv:2301.00474
70. O. V. Dolgov, D. A. Kirzhnits, and E. G. Maksimov, On an admissible sign of the static dielectric function of matter, Rev. Mod. Phys. **53**, 81(1981).
71. S. Ichimaru, Strongly coupled plasmas: high-density classical plasmas and degenerate electron liquids, Rev. Mod. Phys. **54**, 1017(1982).
72. Y. Takada, Excitonic Collective Mode and Negative Compressibility in Electron Liquids, Journal of Superconductivity and Novel Magnetism, **18**, 785(2005).
73. Y. Takada, Emergence of an excitonic collective mode in the dilute electron gas, Physical Review B **94**, 245106(2016).
74. Z. Lin, C. Wang, A. Balassis, J. P. Echeverry, A. S. Vasenko, V. M. Silkin, E. V. Chulkov, Y. Shi, J. Zhang, J. Guo, and X. Zhu, Dramatic Plasmon Response to the Charge-Density-Wave Gap Development in 1T-TiSe2, Phys. Rev. Lett. **129**, 187601 (2022).
75. M. S. Haque and K. L. Kliewer, Plasmon Properties in bcc Potassium and Sodium, Phys. Rev. B **7**, 2416 (1973).
76. P. Knowles, B. Yang, T. Muramatsu, O. Moulding, J. Buhot, C. J. Sayers, E. D. Como, and S. Friedemann, Fermi Surface Reconstruction and Electron Dynamics at the Charge-Density-Wave Transition in TiSe2, Phys. Rev. Lett. **124**, 167602 (2020).

77. D. Varsano, M. Palummo, E. Molinari, and M. Rontani, A monolayer transition-metal dichalcogenide as a topological excitonic insulator, Nature Nanotechnology **15**, 367–372 (2020).

Figures

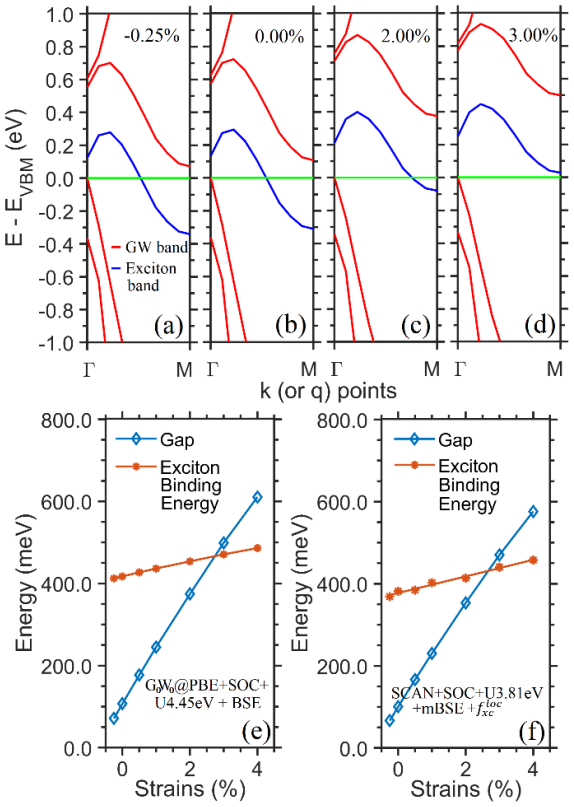


Figure 1. Top row: the quasiparticle and the first exciton band structures obtained from G_0W_0(@PBE+SOC+U4.45 eV)+BSE method along the Γ-M direction of monolayer 1T-TiSe2 under different strains. (a) compressive 0.25%, (b) no-strains, (c) tensile 2% and (d) tensile 3%. The energy of VBM is set to zero. Bottom row: the quasiparticle gaps and the first exciton binding energies at M as a function of strains. (e) results from G_0W_0(@PBE+SOC+U4.45 eV)+BSE and (f) from SCAN+SOC+U (U=3.81 eV) +mBSE+f_{xc}^{loc}.

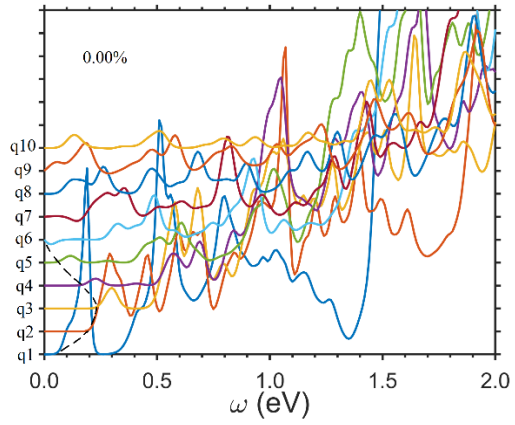


Figure 2. The calculated EELS curves of different momentum transfer of the unstrained monolayer 1T-TiSe2. The onset frequencies of the curves are connected by the dashed black line to show the soft mode like dispersion trend. The curve q1 represents zero momentum transfer of electron and hole, q2 for a momentum transfer of $\frac{1}{9}Q_{\mathrm{M}}$, where Q_{M} is the length from Γ to M in BZ, q3=$\frac{2}{9}Q_{\mathrm{M}}$, q4=$\frac{3}{9}Q_{\mathrm{M}}$, …, and q10=$1.0Q_{\mathrm{M}}$.

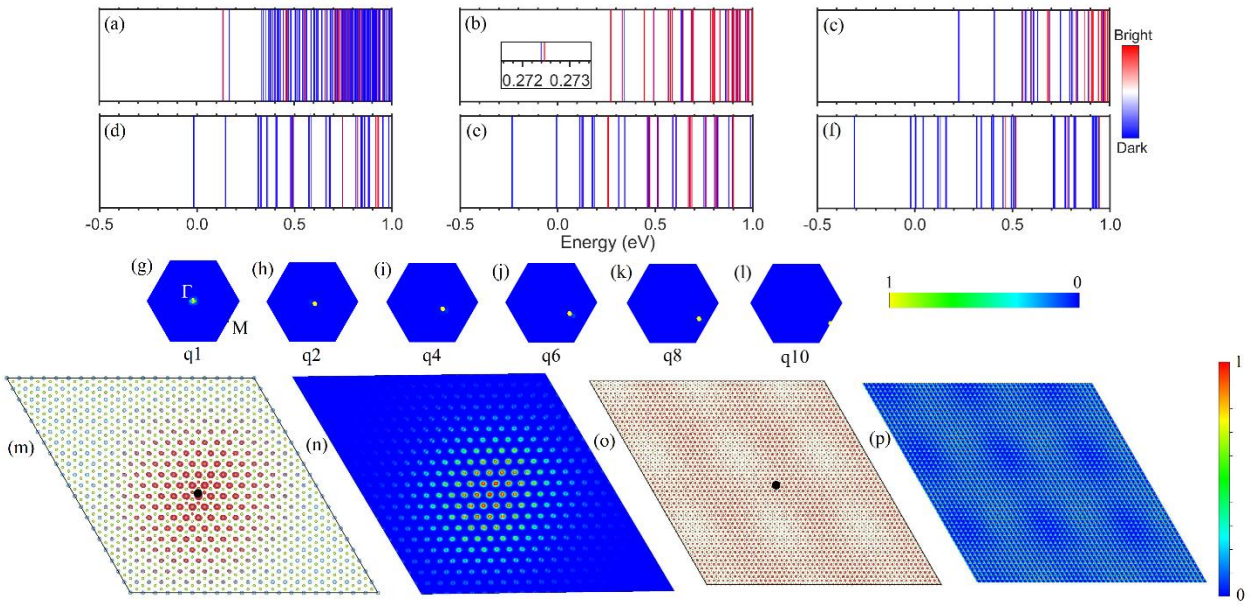


Figure 3. Rows one and two: the exciton spectra of the unstrained monolayer at different momentum transfers with (a) for q1=0, (b) q2=$\frac{1}{9}Q_{\mathrm{M}}$, (c) q4=$\frac{3}{9}Q_{\mathrm{M}}$, (d) q6=$\frac{5}{9}Q_{\mathrm{M}}$, (e) q8=$\frac{7}{9}Q_{\mathrm{M}}$, and (f) q10=$1.0Q_{\mathrm{M}}$. Red for bright excitons and blue for dark ones. The inset in (b) shows the enlarged view of the bright and dark excitons around 0.272 eV. Row three: the band-summed envelope function $\sum_{v,c}\left|A_{vck}^{S}\right|^{2}$ of the first (lowest energy) exciton with (g) for q1=0, (h) for q2, (i) for q4, (j) for q6, (k) for q8 and (l) for q10. The band-summed envelope function $\sum_{v,c}\left|A_{vck}^{S}\right|^{2}$ represents the distribution of the exciton wavefunction in the k space. The hexagons represent the first BZ. The color bar in the third row represents the amplitude scale. Row four: (m) is the modulus squared of the real-space exciton wavefunction of the lowest energy exciton at momentum transfer q1=0. The plot (n) shows the profile of the modulus squared of the real-space wavefunction of the same exciton in a plane close to the Ti atom layer. Plots (o) and (p) are similar plotted and arranged for the lowest energy exciton at q10=$1.0Q_{\mathrm{M}}$. In Row four, the hole positions are denoted as black dots, and the vertical color bar represents the scale in the plots (n) and (p). All plots are for the unstrained 1T-$TiSe_2$ monolayer.